Supplement

The ice-vapor interface during growth and sublimation

Maria Cascajo-Castresana[1], Sylvie Morin[1,2], Alexander M. Bittner[1,3]

[1] CIC nanoGUNE (BRTA), Av. Tolosa 76, 20018 Donostia, Spain

[2] Department of Chemistry, York University, Toronto, ON M3J 1P3, Canada

[3] Ikerbasque Basque Foundation for Science, Plaza Euskadi 5, 48009 Bilbao, Spain

1. Pressure jumps

We used the following pressure jumps to induce growth

$h \approx 1$ to 1.06 at -20.5ºC

$h = 0.97$ to 1.17 at $\geq$ -19ºC

$h \approx 1$ to 1.21 at -18.2ºC

$h = 0.89$ to 0.97 at $\approx$ -18ºC

with h being the relative humidity. The jumps were in each case followed by stabilization at $h \leq 1$, while keeping the sample isothermal. In the jump from 0.89 to 0.97, the temperature shifted (and was recorded for each following image). The maximum jump was hence 21% ($h = 1.21$). The time to adjust the pressure (which is done automatically) was in the range of 10 s.

2. Ice growth speeds

Figure S1 shows a well-resolved hexagonal scalene ice crystal with its basal plane (0001) oriented nearly parallel to the substrate. ESEM allows to determine the growth over time for the nearly vertically oriented prism faces. A growth speed of $\approx$100 nm/s is observed at -18.7ºC and $h = 1.09$ (9% supersaturation).
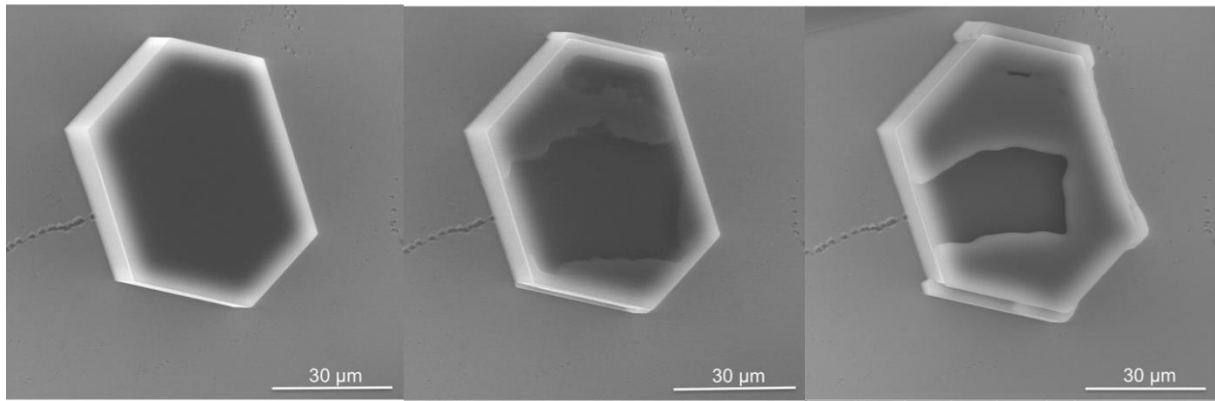
Figure S1: Hexagonal crystal of ice on a clean silicon wafer. The basal plane is nearly horizontal to the substrate. The outer rim is bright, an effect that might indicate charging. ESEM imaging conditions: P = 127.1 Pa, T = -18.7ºC, $Psat$ = 117.0 Pa, h = 1.09. The crystal is scanned again after 87 s and after 227 s, respectively.
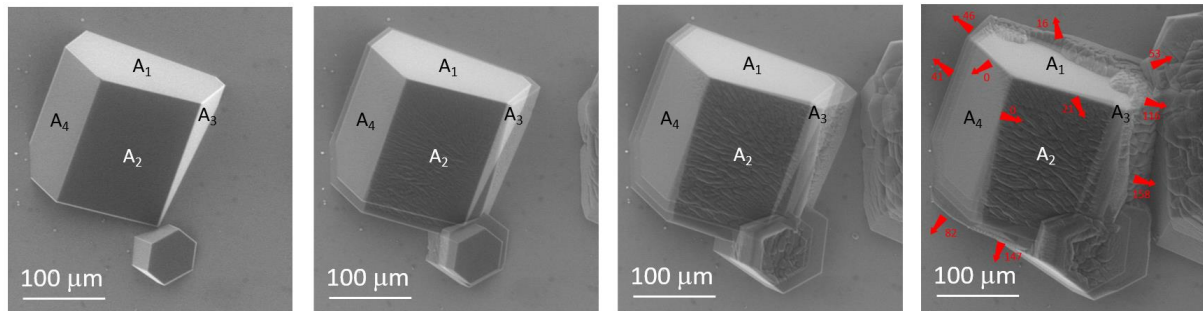

Figure S2: Image series displayed in Fig. 3 (main text) with successive superposition of images (Fig. 3 A to D) as semi-transparent images. Arrows and numbers mark growth directions and growth speeds in nm/s. The speeds are averaged over three to four images. Facets on the largest crystal are labelled A_1 to A_4.

Figure S2 shows a time series at -17.9 ºC and h = 1.03, from which we extracted the growth rates. Various average growth speeds (in nm/s) and directions are marked. The values range from 0 to 158 nm/s. The basal face A_1 grows significantly slower than the prism faces (A_2 to A_4) as expected. The coalescence of isolated crystals complicates the results.

3. Grain boundaries and micrometer-sized pores

The depth or height of the grain boundaries can be estimated by ESEM of tilted samples. We used a high tilt angle (θ = 60°), such that distances measured in the images in the tilt direction are close to depth or height values:

$$height = distance/\sin(\theta) \qquad (S1)$$

Hence for a 60° tilt angle, we find that *depth or height of grain boundaries* is proportional to 1.22×*distance*. From images such as Figure S3 we found values in the range of 7 to 10 µm.
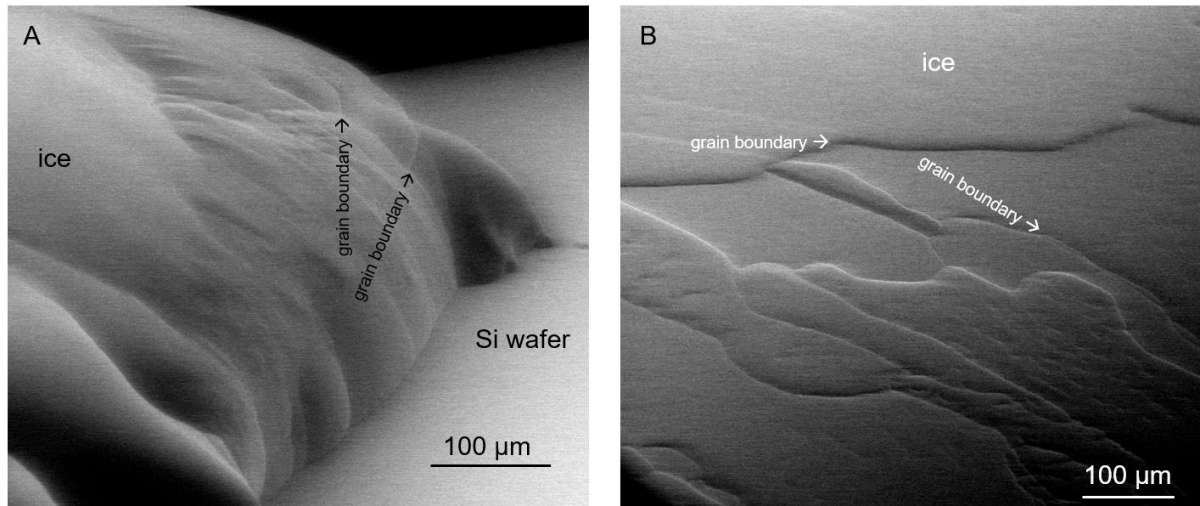

Figure S3: ESEM images of ice layers at -10°C and 260 Pa ($h = 1.00$). Stage tilt 60°

The same images also allow measuring the overall thickness of the deposited ice layers, which was on the order of 200 µm. However, this value must be taken as a minimum value because prolonged growth experiments lead to complete coverage of the Si wafer, and thus loss of our height reference.
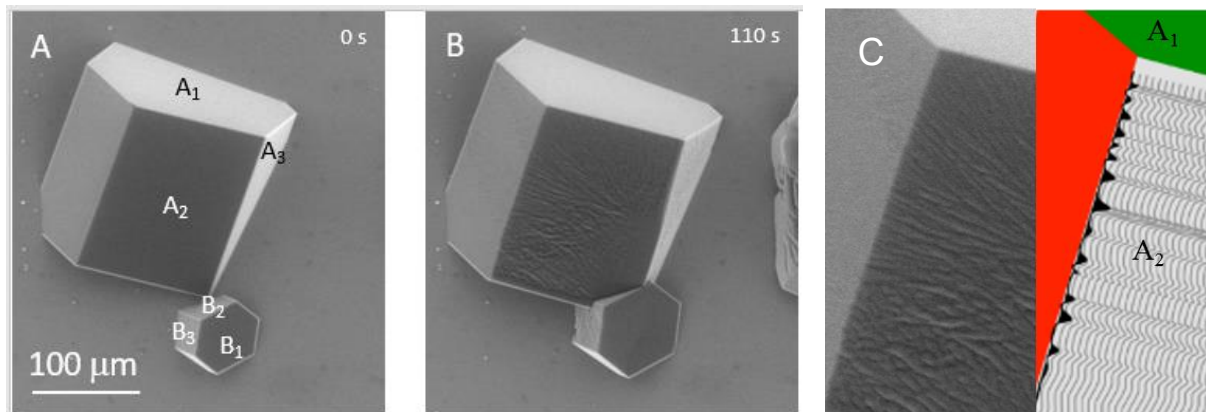

Figure S4: Growing ice single crystal (ESEM images see Figure S2) (Figures A and B) and a zoom into Figure B, with a scheme of the faces A_1, A_2, A_3, just after coalescence with another ice crystal (faces B_1, B_2, B_3) (Figure C).

Figure S4A and S4B shows some details of grain boundaries that develop during the coalescence of two growing crystals (crystal A and crystal B). The scheme in Figure S4C shows the facet A_2 (in white) covered by multiple dislocations (grey wavy lines) meeting perfect facets (in red and green). The truncated dislocation lines form a series of pores observed in

polycrystalline layers. The same observation can be made with polycrystalline ice (Figure S5), although detailed features are sometimes more difficult to see due to the inherent roughness of these films.
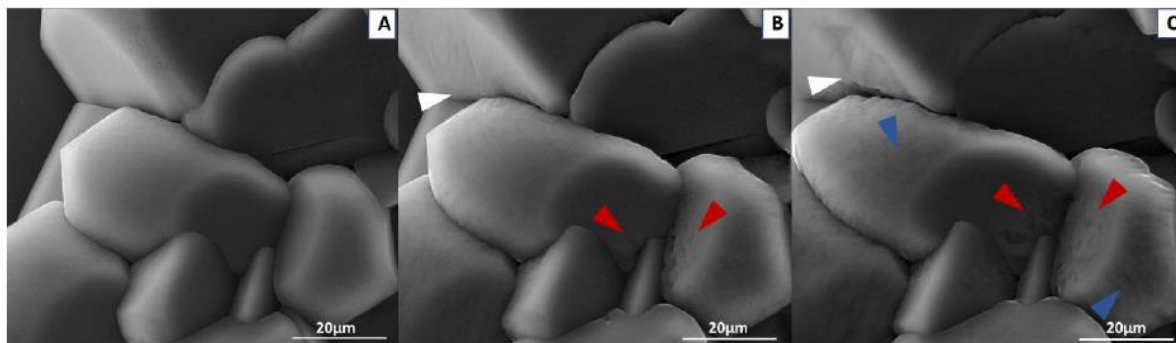

Figure S5: ESEM images of polycrystalline ice during growth. The crystallites progressively lose their smooth flat surface appearance in areas where they come into contact with other crystals (red arrows), but also in areas tens of micrometers away (blue arrows). Imaging conditions in A and B: 110 Pa water vapor, -20.1°C, $h = 1.08$; and in C: 109 Pa, -20.1°C, $h = 1.07$.

4. Contamination

The procedure employed to prepare our Si wafers yield very clean surfaces. In fact they are so clean that we have trouble finding defects or debris for beam adjustment. However, to check for ice surface contamination, we made use an area of the Si surface displaying an unusual large debris as a reference (Figure S6, bright object in the middle). After a cycle of ice growth and sublimation over this particular area, one can establish how much the surface of the Si wafer was modified. Here, we assume that any additional features are from impurities that were deposited over time during the growth and sublimation cycle. It is reasonable to assume that in the case of crystalline ice the impurities are mainly accumulating at the surface of the ice and at grain boundaries instead of being incorporated in its structure. EDX analysis (Figure S6) revealed that our wafer was indeed clean, apart from the Si signal, all other peaks were close to the noise level, except for oxygen (from the oxidized surface, hence dominating) and carbon (presumably beam damage during EDX). The particles, analyzed under identical EDX conditions, revealed carbon and oxygen well above the noise level, with a dominating carbon peak. This combination, typical for organic contaminants, was also found for the dark spots (note that the X-ray intensity above ca 5 eV is extremely small, which hides several possible candidates for metals). It is noteworthy to mention that these features are present also at the surface of the wafer under high vacuum and at ambient temperature after ice growth and sublimation.
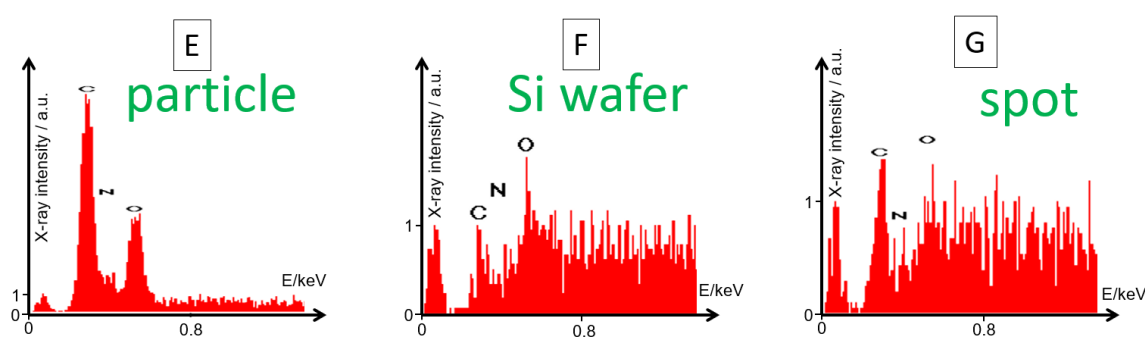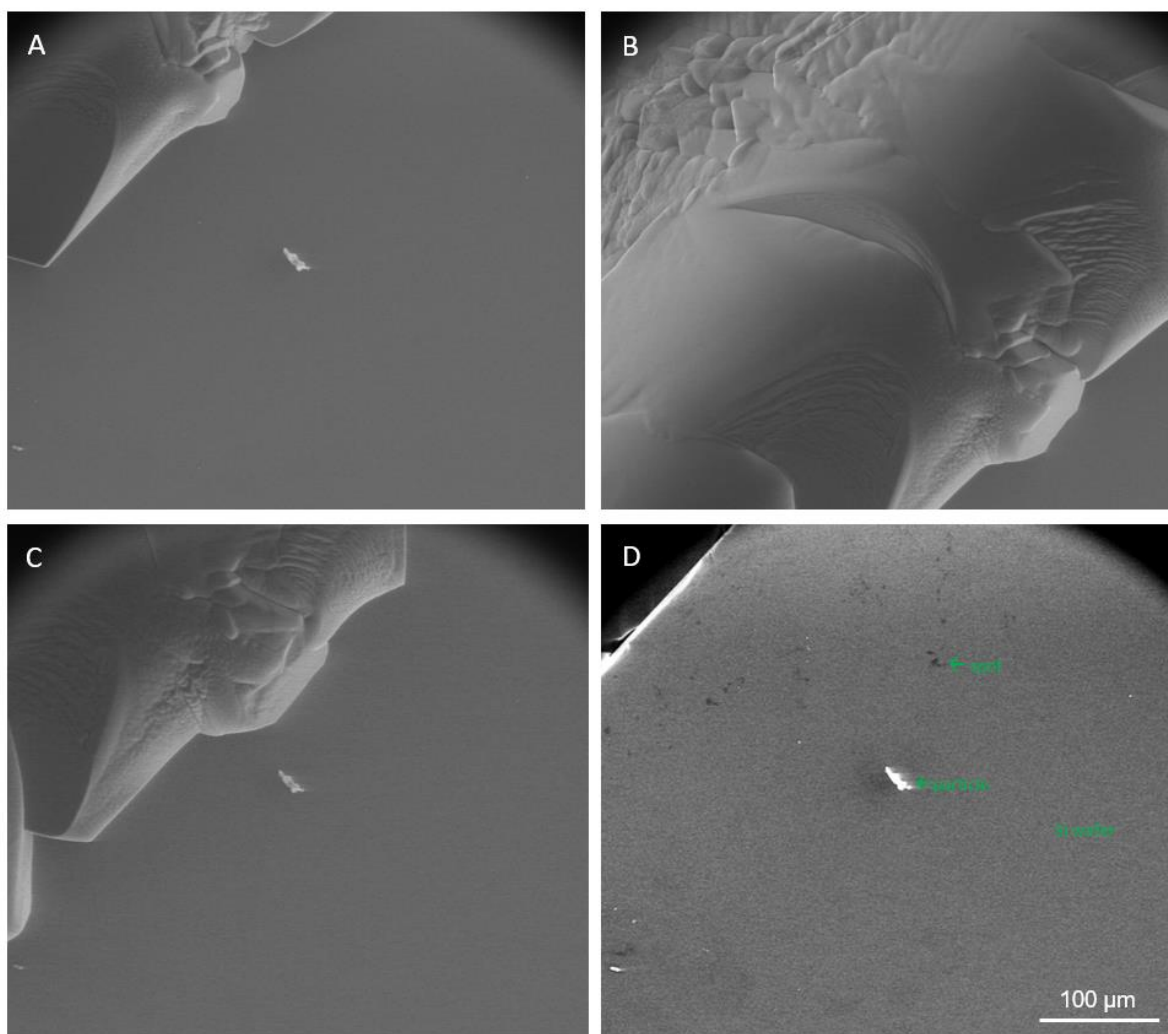
Figure S6. ESEM with a 10 kV beam, imaging at -15°C and 173 Pa ($h = 1.05$) (ice front appearing) (A), 173 Pa (ice covering almost the whole surface) (B), and 170 Pa ($h = 1.03$) (ice front receding) (C). Final image (no ice): -14.9 °C, 165 Pa ($h = 1.00$) (D). The scale bar is the same for all images. EDX data: Obtained from (D) over three different types of features (E, F, G). The EDX exhibits huge intensity for Si ($Z = 14$) at 1.74 keV, which is removed for better visualization of the low energy range. There is no signal for $Z = 9$ to 13. $Z = 8$ to 6 is marked for oxygen, nitrogen and carbon. Below 0.1 keV the spectrum shows artefacts.

In an attempt at quantifying the amount of contamination, we estimated that the dark spots cover only ≈1% of the surface. Based on EDX signals we estimate that the features associated with contaminants are of a similar thickness as that of a Si oxide layer (2 nm; the EDX signals shows peaks just above the noise level for C and O). The height of the ice layer, which covers almost 100% of the surface, is about 20 µm at this very early state of a growth experiment. This yields an estimate of 10^{-6}=1 ppm of contaminants. However, the white dots/particles seen in Fig. 5D and F are at least equally important: assuming a spherical shape, they give higher values (due to the much larger height). Counting five series of ice-overgrown areas (see Fig. S6) and comparing volumes of the dots associated to contaminants with estimated ice volumes gave an estimate of tens of ppm, i.e. ten times higher than the value estimated for the dark spots. These estimates support the notion that these contaminants (bright dots and dark spots) are not acting as nuclei or pinning centers for the creation of asperities in the ice surface during sublimation (see main text and Fig. 5).

5. Beam damage

Various mechanisms can cause beam damage (Egerton et al., 2004; Royall et al., 2001), generally, X-rays appear to cause more problems than electrons (Henderson, 1995). Beam damage should be minimized, for which imaging of areas in the micro- rather than in the nano-range was sufficient. Indeed, the standard procedures cause negligible damage. It is, however, difficult to assess damage after longer imaging because the ice surfaces are highly dynamic (see below). Given the delicate nature of ice, the absence of damage had to be verified by specific experiments, as detailed in the following.

J.M. Alonso et al. already showed that the conditions employed here are safe for about 1 min even on sensitive proteins (Alonso et al., 2013), hence doses could be increased by zooming in, which was otherwise avoided. Only for image sizes of ca. 10 µm changes became obvious, e.g. darkening of areas. Zooming out thereafter allowed imaging the created defect, showing up as dark micro-spot on the grey, rather flat ice surface. The data show nearly complete healing of the damaged areas (micro-spots) after several minutes, due to the dynamic nature of the ice (see Figure S7).
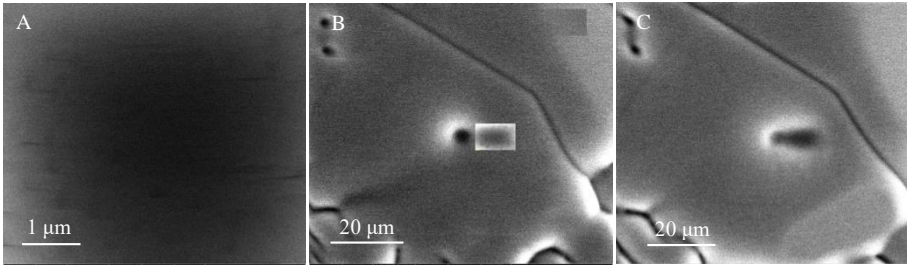
Figure S7: Effects of exposing an ice surface to a 10 keV beam at constant dwell time (20 µs) for several seconds. (A) Zooming in a small area shows a dark microspot. The horizontal streaks might be very fast submicrospots. (B), (C) After two identical consecutive scans of the same area, a deep hole (dark spot) appears. The beam is then zoomed in again on the rectangular window. (C) The small rectangular area has caused more damage (marked with red triangle). Imaging conditions: 287 Pa, -10.3 ºC, h = 1.13.

Another example for typical scan damage on a polycrystalline ice surface is provided in Figure S8. Each rectangle corresponds to a smaller image recorded before; after zooming out the damaged area can be easily detected.
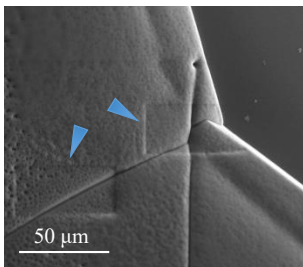

Figure S8: Beam damage to a polycrystalline ice surface. Characteristic rectangle structures caused by the beam are marked with blue triangles. Imaging conditions: 113 Pa, -20.0 ºC, h = 1.07 (10 kV, emission current at FEG 204 µA, current on sample ca. 1 nA, frame time 29.6 s, 1024x884 pixels, dwell time 20 µs)

Such defects must be related to mass loss. From an electron beam, one would expect sputtering, which, however, is known to occur only at higher voltages (Egerton et al., 2004). Another possibility is heating, which is based on the deceleration of the electrons in the solid ice (Egerton et al., 2004; Royall et al., 2001). In SEM samples the energy can be very well dissipated (in three dimensions). The temperature change for local heating of a stationary beam is (Egerton et al., 2004)

$$\Delta T = 3IU/(2\pi\kappa R) \qquad (S2)$$

where I is the beam current (low nA range), U is the beam voltage (max. 10 kV), and κ=1.6 W/(mK) is the thermal conductivity of ice. When R is set to the beam diameter of several nm, one has to include the ratio of dwell time to scan time (>>1000), resulting in negligible temperature changes for the used currents and voltages (see above). Even if repeated scanning of a zoomed-in area (10 µm) is considered as stationary, the temperature would increase by a

mere 0.55 K (this would also be expected for heating a µm-sized interaction volume). So local melting or temperature-induced sublimation is not expected under any condition in our SEM samples, in contrast to TEM samples, e.g. nanoscale voids in thin layers (Mirsaidov et al., 2012). Such small volumes can be approximated by thermally isolated samples ($\kappa = 0$). Even in this case, our beam power would be just about sufficient for melting microparticles:

$$dose = I \cdot t / A_p \quad \text{(S3)}$$

with beam current I, dwell time t per pixel, and pixel area A_p

$$energy = I \cdot t \cdot U \quad \text{(S4)}$$
$$power = I \cdot U \quad \text{(S5)}$$

with beam voltage U. For our standard parameters, $I = 1.6$ nA, $t = 3$ ms, $A_p = (30\ \mu m)^2/(1024 \cdot 884)$, $U = 20$ kV, the energy is 96 nJ. The ice melting enthalpy of 330 MJ/m^3 is much larger than the enthalpy of heating the ice up to 0 ℃, which we neglect. We could thus merely melt an ice cube of 6.6 µm side length.

We thus postulate that the damage of ice in ESEM is caused by radiolysis, i.e. based on chemical rather than thermal changes. Radiolysis can cause structural changes in ice, which ultimately extend to areas that are much larger than the beam diameter. Scanning at very short dwell times (0.1 µs) revealed constant formation and disappearance of sub-micro-depressions of ca. 300-500 nm in diameter. These small spots are visualized in Figure S7A as horizontal streaks. They have low contrast, but they are the precursors of the dark micro-spots, like the one filling the complete image of Figure S7A. This finding has, to our knowledge, not been reported before. It should be connected to the stochastic nature of the damage spurs around the beam track (Royall et al., 2001), although the spots themselves are much larger than spurs (10 nm). The lifetime of spurs is in the ms range. The used fast scans fit well to this estimate (dwell time in the low µs range, ≈200 pixels per line, one spot ca. 5 lines, hence < 1 ms are necessary to image a spot as a disk, and not as a streak).

The radius R_{dam} of the circular heavily damaged area can be computed from the depth of the damaged spur, which is taken as the diameter of the damaged volume. Castaing's rule (Yung et al., 2015) for oxygen (water) yields

$$R_{dam}/\mu m = 0.066 \cdot (U/keV)^{1.7} - 0.022 \qquad (S6)$$

for water (oxygen, $Z = 8$, and minimal electron absorption energy = 0.525 keV). Our voltage range gives 1 µm to 11 µm.

We note that in typical SEM experiments, zooming out after prolonged imaging of small areas might result in the visualization of typical carbon deposits. We never observed such structures, albeit they should survive ice sublimation. The oxidative nature of ionized water in ESEM, e.g. the prevalence of OH radicals (Royall et al., 2001), likely removes carbon deposits very fast. This effect can be used for electron beam structuring of polymers (Toth et al., 2007).

References

Alonso, J. M., Górzny, M. L. & Bittner, A. M. The physics of tobacco mosaic virus and virus-based devices in biotechnology. *Trends Biotechnol.* **31,** 530–538 (2013). https://doi.org/10.1016/j.tibtech.2013.05.013

Egerton, R. F., Li, P. & Malac, M. Radiation damage in the TEM and SEM. *Micron* **35,** 399–409 (2004). https://doi.org/10.1016/j.micron.2004.02.003

Henderson, R. The potential and limitations of neutrons, electrons and X-rays for atomic resolution microscopy of unstained biological molecules. *Quarterly Reviews of Biophysics* **28,** 171–193 (1995). https://doi.org/10.1017/S003358350000305X

Mirsaidov, U., Ohl, C.-D. & Matsudaira, P. A direct observation of nanometer-size void dynamics in an ultra-thin water film. *Soft Matter* **8,** 7108–7111 (2012). https://doi.org/10.1039/C2SM25331C

Royall, C. P., Thiel, B. L. & Donald, A. M. Radiation damage of water in environmental scanning electron microscopy. *J. Microsc.* **204,** 185–195 (2001). https://doi.org/10.1046/j.1365-2818.2001.00948.x

Toth, M., Lobo, C. J., Knowles, W. R., Phillips, M. R., Postek, M. T. & Vladár, A.E. Nanostructure Fabrication by Ultra-high Resolution Environmental Scanning Electron Microscopy. *Microsc. Microanal.* **7,** 525–530 (2007). https://doi.org/10.1021/nl062848c

Yung, L. C., Fei, C. C., Mandeep, J. S., Amin, N. & Lai, K. W. Bulk substrate porosity verification by applying Monte Carlo modeling and Castaing's formula using energy-dispersive x-rays. *J. Electron. Imaging* **24,** 61105 (2015). https://doi.org/10.1117/1.JEI.24.6.061105